ChemPubSoc Europe
DOI: 10.1002/cplu.201402394
CHEMPLUSCHEM
Full Papers

# $Bi_2O_3$@Reduced Graphene Oxide Nanocomposite: An Anode Material for Sodium-Ion Storage

Chandrasekaran Nithya*[a]

The high capacity, excellent cyclability, and good rate capability of reduced graphene oxide (rGO) anchored with $Bi_2O_3$ nanocomposite for sodium-ion batteries is reported. A simple reduction method is adapted to deposit spherical $Bi_2O_3$ nanoparticles on the surface of rGO sheets. The surfactant cetyltrimethylammonium bromide (CTAB) plays a major role in controlling the morphology of the $Bi_2O_3$ nanoparticles. This $Bi_2O_3$@rGO nanocomposite has the advantages of high reversible capacity with a capacity retention (at high rate) of 70.2% after 200 cycles at a current density of 350 mA g$^{-1}$. This superior performance can be attributed to the fact that rGO sheets hamper the volume expansion of $Bi_2O_3$ nanoparticles and result in faster diffusion of $Na^+$ ions (diffusion coefficient: $5.12\times10^{-8}$ cm$^2$ s$^{-1}$) and smaller internal resistance (84.17 Ω) compared with pristine $Bi_2O_3$ nanoparticles. The results suggest that anchoring rGO sheets with metal oxides is one of the simplest ways to enhance the electrochemical performance of sodium-ion batteries.

## Introduction

Increasing demand for energy and growing environmental threats, such as $CO_2$ pollution and global warming, are forcing us to find alternative energy-storage technologies to replace conventionally used fossil fuel resources. Lithium-ion batteries are more suitable than other battery technologies as energy-storage devices to satisfy the current energy crisis. The electric vehicles market and portable electronics are dominated by lithium-ion batteries owing to their high energy and power density.[1,2] However, the demand for lithium-ion batteries has increased and the limited lithium sources are not sufficient to meet future energy requirements. The next possible alternative candidate to replace lithium is sodium,[3] which is more abundant and cheaper than lithium, particularly for large-scale applications. However, the opportunity to explore electrode materials is less than that of lithium batteries because the large ionic size of the $Na^+$ ion (1.02 Å)[4] does not facilitate intercalation/deintercalation into structures in the same way as lithium-ion batteries. Hence, this provides an opportunity to explore new electrode materials for sodium-ion batteries.

Petroleum coke[5] was the first anode material to be investigated for sodium-ion batteries. This material generates a reversible capacity of 85 mA h g$^{-1}$. In 2000, Stevens and Dahn made a significant contribution to the development of sodium-ion batteries, with which they achieved a reversible capacity of 300 mA h g$^{-1}$ when using hard carbon as an anode material.[6] Various types of anode materials, such as carbonaceous materials, metals, metal oxides and their composites, titanium-based oxides, and organic anode materials, have subsequently been investigated for sodium-ion storage.[7–18] However, the challenges associated with sodium-ion batteries are cyclability and rate capability, which restricts meeting the need for a high energy density. The reason for failure in the carbon-based anode material is that the $Na^+$ ion is large, so it cannot intercalate/deintercalate easily between graphitic layers.[19,20] Metals, metal oxides and intermetallic alloys, are successfully developed as anode materials for lithium- and sodium-ion batteries. However, these materials suffer from severe volume expansion during cycling, which leads to mechanical failure in the anode materials. For example, Gu et al. reported the failure mechanism of $SnO_2$ nanowires for sodium-ion batteries in which alloying/dealloying resulted in pores, which led to a structure of tin particles confined in a hollow matrix of $Na_2O$.[21] These pores greatly enhance the electrical impedance and result in poor cyclability of $SnO_2$. To overcome these kinds of issues in anode materials, highly conductive reduced graphene oxide (rGO), the in-plane electrical conductivity[22] of which is 5880 S cm$^{-1}$, has been used as a matrix to hold the active anode materials during cycling. Recently, bismuth-based oxide (*p*-$Bi_2O_3$/Ni) and sulfide materials have shown superior electrochemical performance for lithium-ion batteries[23–25] To the best of my knowledge, no reports are available to date on $Bi_2O_3$ anode material for sodium-ion batteries. Herein, for the first time, $Bi_2O_3$/rGO composite anode material has been investigated for sodium-ion batteries, in which the rGO matrix greatly enhances the cycling stability of $Bi_2O_3$ anode material.

## Results and Discussion

Figure 1 shows the XRD patterns of graphene oxide (GO), $Bi_2O_3$, and rGO/$Bi_2O_3$ (1:5) anode materials. The XRD pattern of GO depicts the main peak reflection centered at $2\theta=10.61^\circ$,

---

[a] *Dr. C. Nithya*
*Department of Energy and Environment*
*National Institute of Technology*
*Tiruchirappalli 620 015 (India)*
*E-mail: nithyajcs@gmail.com*

Supporting information for this article is available on the WWW under http://dx.doi.org/10.1002/cplu.201402394.

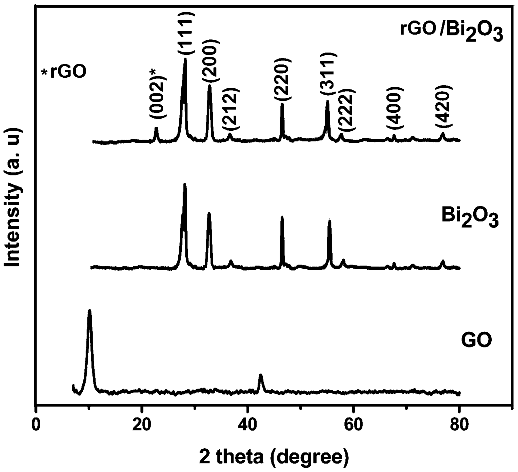

**Figure 1.** XRD patterns of GO, $Bi_2O_3$, and rGO/$Bi_2O_3$.

which is consistent with that reported in the literature.[26,27] All peaks of $Bi_2O_3$ match well with the standard ICDD pattern (ICDD file no. 00-001-0709). The rGO/$Bi_2O_3$ (1:5) composite XRD pattern reflects both phases of rGO and $Bi_2O_3$, in which the peak centered at $2\theta = 24.87^\circ$ corresponds to the formation of rGO[28] (reduction of GO to rGO by using $NaBH_4$) in the synthesized composites. The XRD pattern of the rGO/$Bi_2O_3$ composite does not show any impurity peaks, and also the absence of the peak at $2\theta = 10.61^\circ$ indicates that the reducing agent completely reduces the GO phase to rGO. The rGO content (15% in the composites) in the synthesized composite is determined by thermogravimetric analysis (TGA)/differential thermal analysis (DTA; Figure S1 in the Supporting Information).

Figure S2 in the Supporting Information presents SEM images of GO, $Bi_2O_3$ without adding CTAB, $Bi_2O_3$ with CTAB, and rGO/$Bi_2O_3$ composite anode materials. The SEM image of GO (Figure S2a in the Supporting Information) shows the micron-sized flake-like morphology, which appears as randomly arranged flakes on top of each other. The size of the flakes varies from 0.5 to 2 μm. Figure S2b in the Supporting Information clearly depicts that $Bi_2O_3$ particles synthesized without CTAB appear as irregularly shaped and sized particles with serious agglomeration (particle size $>2$ μm). Figure S2c in the Supporting Information presents a SEM image of the $Bi_2O_3$ material (with CTAB), which has a spherical morphology with a small degree of agglomeration and a particle size of around 200 nm. Thus, it can be clearly understood that the CTAB surfactant controls the morphology and size of the synthesized particles. According to Li et al.,[29] interactions between the surfactant molecules and precursors contribute to the formation of homogeneous nanosized particles. The SEM image of the rGO/$Bi_2O_3$ composite (Figure S2d in the Supporting Information) clearly shows $Bi_2O_3$ particles and rGO sheets, in which the $Bi_2O_3$ particles exist on the surface of rGO sheets. The particle size is about 10–100 nm. Figure 2 shows TEM images and selected-area electron diffraction (SAED) patterns of $Bi_2O_3$ and rGO sheets. The size of the $Bi_2O_3$ particle is around 10–20 nm. The TEM image of rGO clearly shows the layer by layer assembly of sheets arranged together and the sizes of the sheets are about 100 nm. Evidence obtained from the TEM image of the rGO/$Bi_2O_3$ composite (Figure 2e), in which the particle size is around 10–20 nm, also clearly depicts the rGO sheets and $Bi_2O_3$ particles. This is further confirmed by the SAED pattern of the rGO/$Bi_2O_3$ composite. This pattern contains bright and dim rings that correspond to the rGO sheets and $Bi_2O_3$ particles. The *d* spacings calculated from the SAED patterns are 1.391 (400), 1.952 (220), and 2.763 (200) Å for $Bi_2O_3$ and 3.621 Å (002) for rGO,[26] which are in close agreement with JCPDS file no. 52-1007 (for $Bi_2O_3$). The above results are consistent with XRD observations.

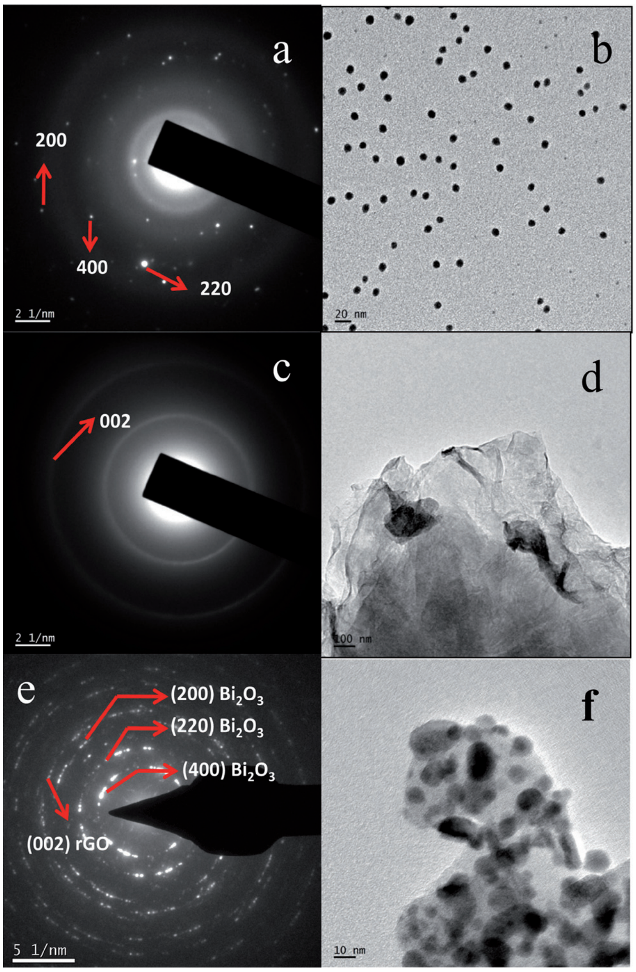

**Figure 2.** SAED patterns of $Bi_2O_3$ (a), rGO (c), and rGO/$Bi_2O_3$ (e). TEM images of $Bi_2O_3$ (b), rGO (d), and rGO/$Bi_2O_3$ composite (f).

Laser Raman spectroscopy is an essential tool and strongly sensitive to graphene and graphene-based materials.[30,31] Usually, two modes of vibration are observed for carbon-based materials, namely, D ($A_{1g}$ mode) and G (owing to first-order scattering of the $E_{2g}$ phonon) bands. The D and G bands correspond to $sp^3$- and $sp^2$-hybridized carbon atoms, respectively, in which the D band is related to a disordered mode and the G band related to an ordered mode. Figure 3 shows the laser Raman spectra of GO and rGO/$Bi_2O_3$ composites. Two bands are observed in the laser Raman spectrum of GO, in which the D band is centered at $\tilde{\nu} = 1349\ cm^{-1}$ and the G band is at $\tilde{\nu} =$

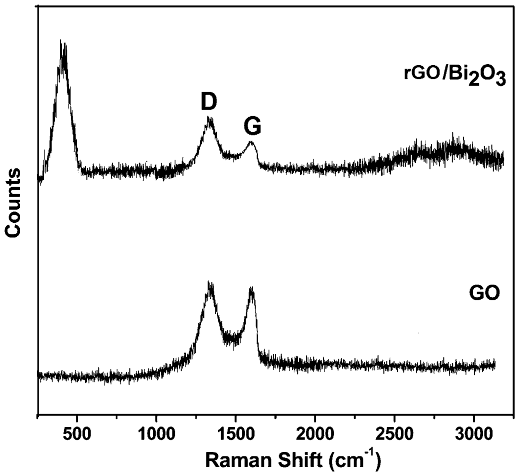

**Figure 3.** Laser Raman spectra of GO and rGO/Bi$_2$O$_3$ nanocomposite.

1583 cm$^{-1}$. These two bands are slightly redshifted in the laser Raman spectrum of the rGO/Bi$_2$O$_3$ composite material. The D band is observed at $\tilde{\nu} = 1355$ cm$^{-1}$ and the G band is at $\tilde{\nu} = 1591$ cm$^{-1}$ in the composites in which the intensity of D band increases after reduction. The intensity ratio of these two bands ($I_D/I_G$) is extensively used to determine the degree of disorder in graphene-related materials. This is because GO sheets may split into smaller domains, which means that more defects will be created after reduction. From these observations, we can confirm that most of the oxygenated groups are removed from the GO domains; therefore, the vacant sites are created owing to oxygen vacancies in the lattice, which results in defects in the rGO sheets.

Figure 4a shows the initial charge/discharge profiles of Bi$_2$O$_3$, rGO, and rGO/Bi$_2$O$_3$ anodes cycled between the potential limits of 0.01 and 2.0 V at a current density of 140 mA g$^{-1}$. For bare rGO, the specific charge capacity is 501 mA h g$^{-1}$, whereas pristine Bi$_2$O$_3$ exhibits a charge capacity of 600 mA h g$^{-1}$. The irreversible capacity loss in the first cycle is 528 and 497 mA h g$^{-1}$ for rGO and Bi$_2$O$_3$, respectively. The rGO/Bi$_2$O$_3$ nanocomposite demonstrates the highest charge capacity of 669 mA h g$^{-1}$, which is almost 97 % of the theoretical capacity, whereas the irreversible capacity loss is only 227 mA h g$^{-1}$. The irreversible capacity losses are attributed to the electrolyte undergoing a reaction with the active sites and decomposition of the electrolyte taking place on the electrode surface to form a solid–electrolyte interface (SEI) in the first charge/discharge process.[32–34] According to Dahn et al.,[35] the irreversible capacity loss of metal oxides is due to the formation of Li$_2$O on the surface of the anode, which consumes lithium and forms a metallic phase. The conversion reaction of Bi$_2$O$_3$ with Na is expected to proceed as shown in Equation (1).

$$Bi_2O_3 + 12\,Na \rightarrow 3\,Na_2O + 2\,Na_3Bi \quad (1)$$

According to the groups of Li[23] and Jung,[26] complete conversion of Bi$_2$O$_3$ with Li should involve 12 Li ions, so the theoretical capacity of Bi$_2$O$_3$ is calculated to be 690 mA h g$^{-1}$. Similar to Li insertion, Bi$_2$O$_3$ also undergoes an alloying reaction with Na$^+$ ions and consumes 12 Na ions, so the theoretical capacity of Bi$_2$O$_3$ for sodium-ion batteries is calculated to be 690 mA h g$^{-1}$. Compared with pristine Bi$_2$O$_3$ and rGO, the composite rGO/Bi$_2$O$_3$ exhibits a high charge capacity, which is attributed to the smaller particles of rGO/Bi$_2$O$_3$ decreasing the sodium-ion diffusion path length; thereby increasing the charge capacity. The poor capacity of pristine Bi$_2$O$_3$ is due to the presence of agglomerated larger particles, which slightly hinder Na$^+$ diffusion; thereby decreasing the charge capacity.

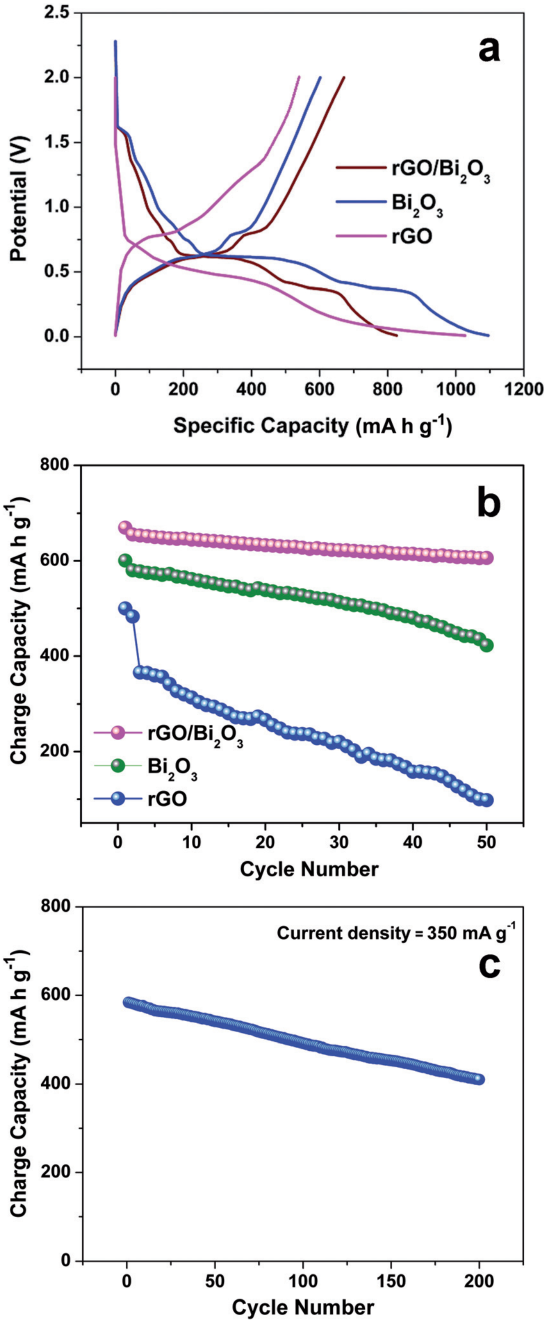

**Figure 4.** a) Charge/discharge curves. b) Cycling performance at a current density of 140 mA g$^{-1}$. c) Cycling performance of rGO/Bi$_2$O$_3$ over 200 cycles.

Figure 4 b depicts the cycling performance of $Bi_2O_3$, rGO, and rGO/$Bi_2O_3$ composites over 50 cycles at a current density of 140 mA $g^{-1}$. The 50th cycle charging capacities of $Bi_2O_3$, $Bi_2O_3$ without CTAB (Figure S3 in the Supporting Information), rGO, and rGO/$Bi_2O_3$ are 417, 310, 102, and 607 mA h $g^{-1}$, respectively; the corresponding capacity retentions are 69.5, 59.3, 20.3, and 89.8 %, respectively. The poor performance of $Bi_2O_3$ is ascribed to the fact that it suffers from crumbling and pulverization, and consequent disconnection with the current collector results in fast capacity fading[36–38] The capacity retention of rGO is also poor compared with those of $Bi_2O_3$ and rGO/$Bi_2O_3$ owing to restacking of rGO sheets during the charge/discharge process. This consumes a large amount of $Na^+$, which reduces the charge/discharge capacity in subsequent cycles. The capacity fading of the rGO/$Bi_2O_3$ composite is 9.26 %. Furthermore, the cell was cycled up to 200 times (Figure 4 c) at a current density of 350 mA $g^{-1}$. After 200 cycles, the cell retains a reversible charge capacity of 413 mA h $g^{-1}$, which is approximately 70 % of the initial charge capacity. This outstanding performance of the rGO/$Bi_2O_3$ nanocomposites is ascribed to the unique spherical morphology of the material. From TEM observations (Figure 2 e), it can be clearly understood that the $Bi_2O_3$ nanoparticles are embedded in flexible rGO sheets. Figure 5 a shows the ex situ XRD pattern of the rGO/$Bi_2O_3$ electrode after the first charging cycle (alloying). The pattern matches well with the *P*$6_3$/*mmc* space group,[39] and it confirms the formation of $Na_3Bi$. The cycled (after 200 cycles) rGO/$Bi_2O_3$ electrode was further examined with ex situ TEM, as shown in Figure 5 b and c. It can be clearly observed that the original morphology of the rGO sheets is preserved; however, the shape of the $Bi_2O_3$ particles is slightly altered owing to the reaction with $Na^+$ ions. This enhanced performance is due to the nanocrystalline nature of $Bi_2O_3$ and flexible rGO sheets contributing to the alleviation of stress and crumbling of the electrode active materials, which results in high capacity and capacity retention. Furthermore, the flexible rGO sheets also act as a conductive matrix for electron transfer during the charge/discharge process. As a result, the electrode architecture can be sustained during cycling, which improves the sodium-ion storage capability.

Figure 6 a and b presents the rate capability curves and cycling performance of the rGO/$Bi_2O_3$ composite at different current densities. It delivers different capacities at different current densities, namely, 678 mA h $g^{-1}$ at 140 mA $g^{-1}$, 581 mA h $g^{-1}$ at 350 mA $g^{-1}$, 562 mA h $g^{-1}$ at 700 mA $g^{-1}$, and 529 mA h $g^{-1}$ at 1400 mA $g^{-1}$. Even after 40 cycles, it delivers 213 mA h $g^{-1}$ at a high current density of 3500 mA $g^{-1}$. The same cell was cycled again at a current density of 140 mA $g^{-1}$; it recovered the original capacity of 670 mA h $g^{-1}$, even after 50 cycles. From this, it can be clearly understood that the rGO/$Bi_2O_3$ nanocomposite withstand high rate cycling.

Figure 6 c shows the cyclic voltammograms of $Bi_2O_3$ and the rGO/$Bi_2O_3$ nanocomposite recorded between 0.01 and 2 V at a scan rate of 0.1 mV $s^{-1}$. Multipeak features (1.64 V (hump) can be observed at approximately 0.63 V (strong peak) in the cathodic region; one strong peak at approximately 0.89 V in the anodic region) indicates that the reaction proceeds between sodium and bismuth oxide in a multistep manner. The peak at 1.64 V corresponds to the reduction of $Bi_2O_3$ to Bi and the strong peak at 0.63 V is attributed to both SEI formation and an alloying reaction between Bi and Na, which forms $Na_3Bi$. Likewise, the peak obtained at 0.89 V in the anodic region corresponds to the dealloying process of $Na_3Bi$ (Figure 5 a), and the broad peak obtained at 1.74 V in the anodic region is attributed to the formation of $Bi_2O_3$ from Bi. The shape of this peak is similar to the peak obtained in the cathodic region, which is ascribed to the $Bi_2O_3$ and rGO/$Bi_2O_3$ anode materials possessing high reversibility. Moreover, the shape of the voltammogram of $Bi_2O_3$ and rGO/$Bi_2O_3$ appears to be

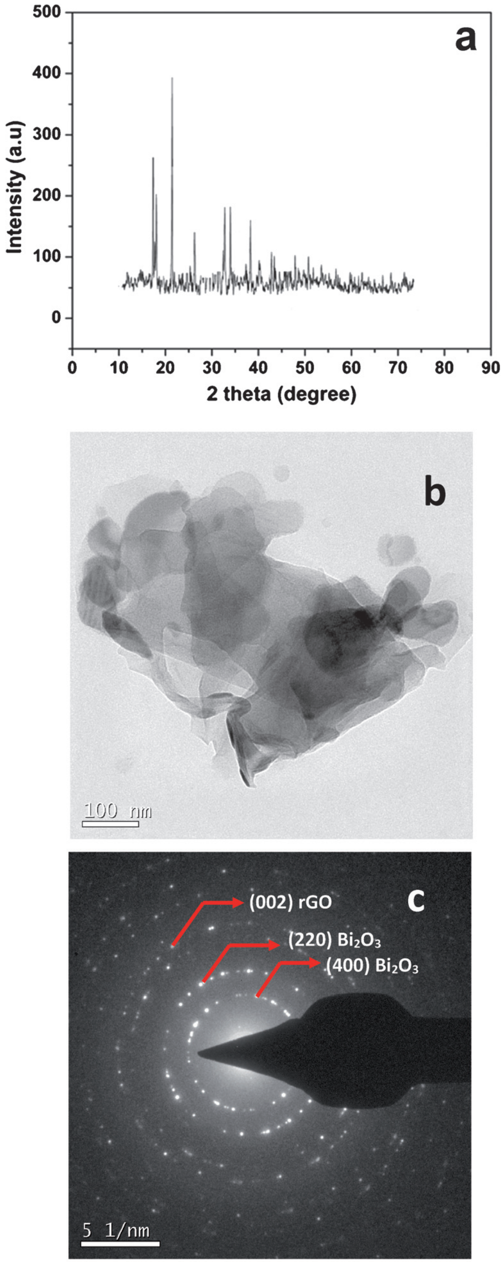

**Figure 5.** a) Ex situ XRD pattern of the rGO/$Bi_2O_3$ composite after the first charging cycle ($Na_3Bi$ formation, *P*$6_3$/*mmc* space group). b) TEM image of the cycled rGO/$Bi_2O_3$ electrode. c) SAED pattern of the cycled rGO/$Bi_2O_3$ electrode.

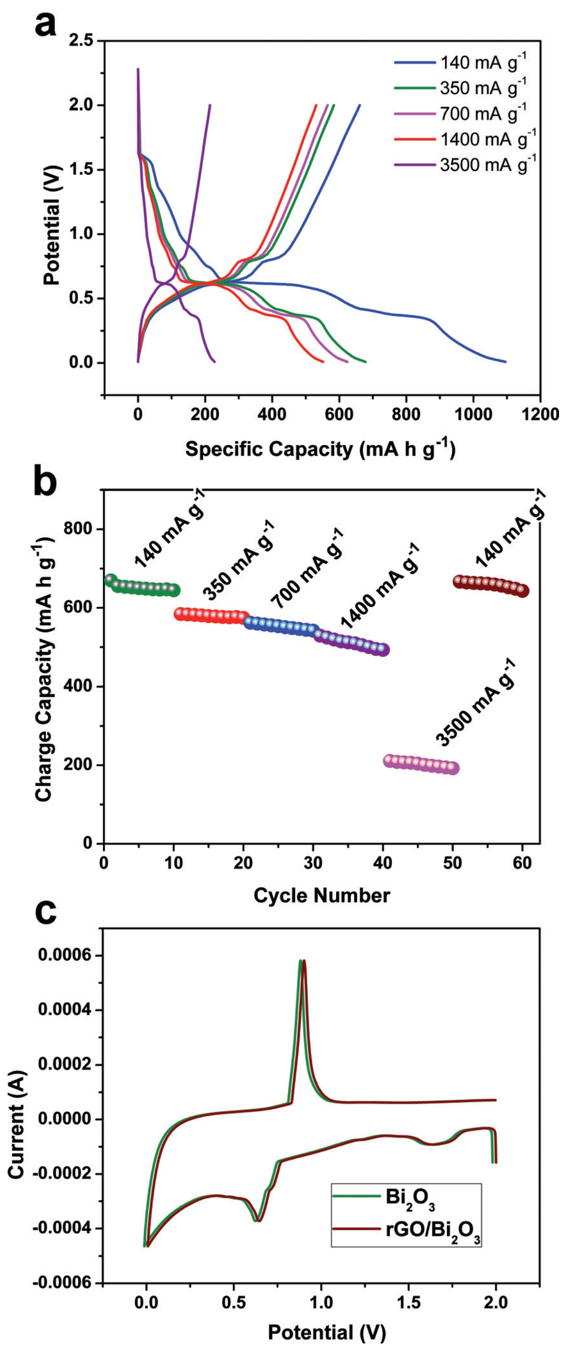

**Figure 6.** a) Charge/discharge curves of rGO/$Bi_2O_3$ at different current densities. b) Rate capability of rGO/$Bi_2O_3$ at different current densities. c) Cyclic voltammogram of $Bi_2O_3$ and the rGO/$Bi_2O_3$ nanocomposite.

almost identical, which clearly reveals that the rGO sheets acts as a matrix that supports the electron-transfer reaction. Thus, $Bi_2O_3$ undergoes the reactions given in Equations (2)–(5) during charging and discharging:

Discharging:

$$Bi_2O_3 + 6\,Na \rightarrow Bi + 3\,Na_2O \quad (2)$$

$$2\,Bi + 6\,Na \rightarrow 2\,Na_3Bi \quad (3)$$

Charging:

$$2\,Na_3Bi \rightarrow 6\,Na + 2\,Bi \quad (4)$$

$$2\,Bi + 3\,Na_2O \rightarrow Bi_2O_3 + 6\,Na \quad (5)$$

Figure 7 shows Nyquist plots of $Bi_2O_3$ and the rGO/$Bi_2O_3$ composite. In each plot there is a semicircle in the high- to medium-frequency range, which characterizes charge-transfer resistance, accompanied by a straight line in the low-frequency region, which corresponds to Warburg impedance owing to diffusion behavior.[40,41] The obtained Nyquist plot is divided into three regions, namely, 1) an intersection in the high-frequency region in the real axis, 2) only one depressed semicircle in the medium-frequency region, and 3) a sloped line in the low-frequency region. Both anodes exhibit similar behavior, except for the size of the semicircle in the medium-frequency region. Z-view software is used to fit the experimental data to simulate the obtained experimental data in the present study (an equivalent circuit is proposed to simulate the obtained experimental data and is shown in Figure S4 in the Supporting Information). The circuit elements are $R_s$ (solution resistance in the bulk electrolyte), $R_{SEI}$ and $C_{SEI}$ (the ionic resistance and capacitance, respectively, present in the SEI layers), $R_{ct}$ and $C_{dl}$ (charge-transfer resistance and double-layer capacitance, respectively, in the electrode–electrolyte interface), and $W$ (the

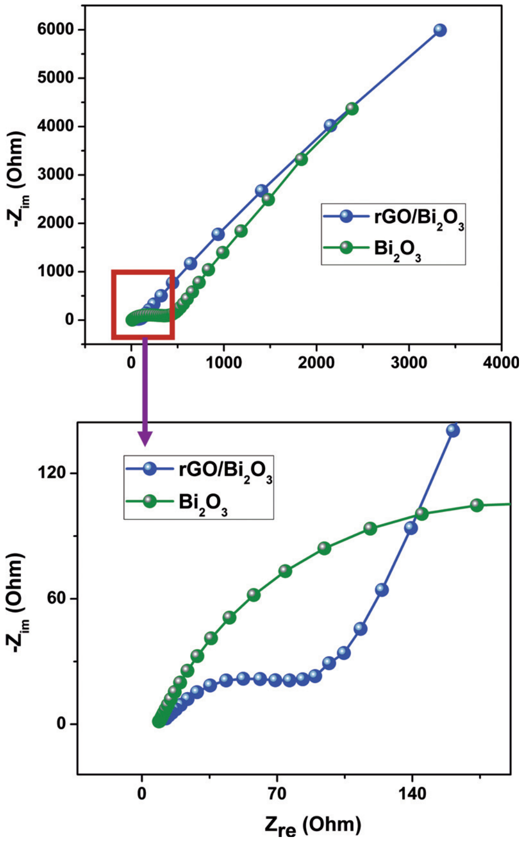

**Figure 7.** Nyquist plot of $Bi_2O_3$ and the rGO/$Bi_2O_3$ nanocomposite.

Warburg element, which characterizes diffusion of $Na^+$ ions). The value of $R_{SEI}$ plays a significant role in determining the overall internal resistance in the cell, which is 380.43 (for $Bi_2O_3$) and 63.93 Ω (for rGO/$Bi_2O_3$). The $R_{ct}$ values of $Bi_2O_3$ and the rGO/$Bi_2O_3$ nanocomposite are 34.16 and 20.24 Ω, respectively. Compared with the electrodes composed of rGO/$Bi_2O_3$ and $Bi_2O_3$, the rGO/$Bi_2O_3$ has a much smaller charge-transfer resistance (84.17 Ω), which indicates that rGO in the composite assists in the reduction of the interfacial charge-transfer resistance.[42] The $Na^+$-ion diffusion characteristics of $Bi_2O_3$ and rGO/$Bi_2O_3$ were calculated by using Equation (6).[43,44]

$$D = \frac{R^2T^2}{2A^2n^4F^4C^2\sigma^2} \tag{6}$$

Here, $R$ is the gas constant, $T$ is the absolute temperature, $n$ is the number of electrons per molecule oxidized, $A$ is the active surface area, $F$ is the Faraday constant, $C$ is the concentration of $Na^+$ ions, $D$ is the diffusion coefficient, and $\sigma$ is the coefficient of Warburg impedance obtained from the intersection of the straight line on the real axis.[44] This equals $R_s+R_{ct}-2\sigma^2C_{dl}$. The diffusion coefficient ($D_{Na}$) value of rGO/$Bi_2O_3$ ($5.12\times10^{-8}$ cm$^2$ s$^{-1}$) is higher than that of the pristine $Bi_2O_3$ anode ($6.18\times10^{-9}$ cm$^2$ s$^{-1}$). The above results confirmed that $Na^+$ ions diffused very easily into the interior sites of rGO/$Bi_2O_3$ network compared with the pristine $Bi_2O_3$ network. This is supported by the fact that formation of a very thick surface film over the active electrodes prevents the diffusion process, as well as effective charge transfer from or to the electrode/electrolyte interface.[45]

## Conclusion

A simple chemical reduction method was followed for the synthesis of the rGO/$Bi_2O_3$ nanocomposite for sodium-ion batteries. The surfactant CTAB played an important role in determining the morphology of the synthesized $Bi_2O_3$ particles. The sizes of the $Bi_2O_3$ particles were in the range of 10–20 nm and anchored well on the surface of the rGO sheets. This kind of embedding of $Bi_2O_3$ particles on the surface of rGO sheets buffered the volume change upon $Na^+$-ion insertion and deinsertion. The nanocomposite exhibited a superior reversible capacity, excellent cyclability, and good rate capability during cycling. This superior performance was attributed to the rGO sheets acting as a conductive matrix during cycling and assisting the fast diffusion of $Na^+$ ions and low impedance. Based on the above results, the present study provides an idea to develop an efficient metal oxide anode for sodium-ion batteries with improved performance.

## Experimental Section

Graphene oxide was synthesized by using a modified Hummers method.[46,47] The rGO/$Bi_2O_3$ composite was synthesized through a simple reduction method by using $NaBH_4$ as a reducing agent. In a typical synthesis, graphite oxide (1 g) was dispersed in distilled water (50 mL) by using an ultrasonicator (Model PG Analytics, 230 V, 50 Hz) for 1 h. The dispersed solution was removed from the sonicator bath and transferred to a magnetic stirrer. $Bi(NO_3)_3\cdot5H_2O$ (7 g) and CTAB (0.5 g) were added to the above GO dispersion under continuous stirring. $NaBH_4$ (10 g) was added dropwise to this mixture and the resulting solid was separated by filtration. For the preparation of pristine $Bi_2O_3$, the same procedure was repeated, but without the addition of GO. After washing with deionized water to remove excess $Cl^-$ ions as well as surfactant and other ions, $Bi_2O_3$ and the rGO/$Bi_2O_3$ composite were obtained by drying for 24 h in vacuo.

TGA (PerkinElemer/TGA4000) of the rGO/$Bi_2O_3$ nanocomposite was analyzed from 0 to 700 °C at a heating rate of 10 °C min$^{-1}$ in air to understand the thermal decomposition behavior, as well as the percentage of carbon present in the composites. The synthesized GO and rGO/$Bi_2O_3$ composites were characterized by means of an X-ray diffractometer (Rigaku Ultima III XRD) at a scan rate of 1 ° min$^{-1}$ by using $Cu_{K\alpha}$ radiation ($\lambda=1.5418$ Å), while the voltage and current were held at 40 kV and 20 mA ($2\theta=10$–80°). The morphology and microstructure of the composites were characterized by means of SEM (VEGA3 SB, TESCAN Instruments) and TEM (FEI-Tecnai-20 G2). Raman spectra were recorded for the synthesized materials in a Renishaw InVia laser Raman microscope with a He–Ne laser ($\lambda=633$ nm).

The anodes (pristine $Bi_2O_3$ and rGO/$Bi_2O_3$ composite) were prepared by mixing 80 wt % prepared composites, 10 wt % Super-P carbon, and 10 wt % polyvinylidene fluoride (PVDF) binder in *N*-methylpyrrolidone (NMP) to form a homogeneous slurry. The slurry was coated on copper foil and dried under ambient conditions. Circular discs with a diameter of 18 mm were punched out and dried in vacuo at 120 °C for 12 h. The mass loading of the active materials for $Bi_2O_3$ and rGO/$Bi_2O_3$ were 1.05 and 1.12 mg cm$^{-2}$, respectively. Finally, coin cells of 2032 type were assembled inside an argon-filled glove box by using the prepared anode as a working electrode, sodium foil as a reference electrode, celgard 2400 as the separator, and $NaClO_4$ in 1:1 ethylene carbonate/propylene carbonate (EC/PC) as the electrolyte. Charge–discharge studies of the coin cells were performed by using a programmable battery tester at a constant current of 140 mA g$^{-1}$ for 50 cycles in the potential range of 0.01–2.0 V. Cyclic voltammograms were recorded by using a Biologic instruments potentiostat/galvanostat at a scan rate of 0.1 mV s$^{-1}$ between 0.01 and 2.0 V. Electrochemical impedance spectra were measured by using a Biologic instruments potentiostat/galvanostat with an alternating current (AC) voltage signal of 5 mV and the frequency range was between 100 kHz and 5 mHz.

## *Acknowledgements*

*The author wishes to thank Department of Science and Technology (DST), India for an INSPIRE Faculty Award.*

**Keywords:** bismuth · electrochemistry · graphene · reduction · sodium

[1] X. Huang, B. Sun, S. Chen, G. Wang, *Chem. Asian J.* **2014**, *9*, 206–211.
[2] C. Nithya, S. Gopukumar, *ChemSusChem* **2013**, *6*, 898–904.
[3] C. Nithya, S. Gopukumar, *J. Mater. Chem. A* **2014**, *2*, 10516–10525.
[4] M. D. Slater, D. Kim, E. Lee, C. S. Johnson, *Adv. Funct. Mater.* **2013**, *23*, 947–958.
[5] M. M. Doeff, Y. P. Ma, S. J. Visco, L. C. Dejonghe, *J. Electrochem. Soc.* **1993**, *140*, L169–170.

[6] D. A. Stevens, J. R. Dahn, *J. Electrochem. Soc.* **2001**, *148*, A803 – A811.
[7] Y. Shao, J. Xiao, W. Wang, M. Engelhard, X. Chen, Z. Nie, M. Gu, L. V. Saraf, G. Exarhos, J. G. Zhang, J. Liu, *Nano Lett.* **2013**, *13*, 3909 – 3914.
[8] T. Matsushita, Y. Ishii, S. Kawasaki, *ECS Trans.* **2013**, *50*, 1 – 6.
[9] J. Qian, Y. Chen, L. Wu, Y. Cao, X. Ai, H. Yang, *Chem. Commun.* **2012**, *48*, 7070 – 7072.
[10] M. K. Datta, R. Epur, P. Saha, K. Kadakia, S. K. Park, P. N. Kumta, *J. Power Sources* **2013**, *225*, 316 – 322.
[11] P. R. Abel, Y. M. Lin, T. Souza, C. Y. Chou, A. Gupta, J. B. Goodenough, G. S. Hwang, A. Heller, C. B. Mullins, *J. Phys. Chem. C* **2013**, *117*, 18885 – 18890.
[12] H. Xiong, M. D. Slater, M. Balasubramanian, C. S. Johnson, T. Rajh, *J. Phys. Chem. Lett.* **2011**, *2*, 2560 – 2565.
[13] D. A. Tompsett, M. S. Islam, *Chem. Mater.* **2013**, *25*, 2515 – 2526.
[14] Q. Sun, Q. Q. Ren, H. Li, Z. W. Fu, *Electrochem. Commun.* **2011**, *13*, 1462 – 1464.
[15] Y. Liu, Y. Xu, Y. Zhu, J. N. Culver, C. A. Lundgren, K. Xu, C. Wang, *ACS Nano* **2013**, *7*, 3627 – 3634.
[16] A. Rudola, K. Saravanan, S. Devaraj, H. Gong, P. Balaya, *Chem. Commun.* **2013**, *49*, 7451 – 7453.
[17] Y. Park, D. S. Shin, S. H. Woo, N. S. Choi, K. H. Shin, S. M. Oh, K. T. Lee, S. Y. Hong, *Adv. Mater.* **2012**, *24*, 3562 – 3567.
[18] R. R. Zhao, Y. L. Cao, X. P. Ai, H. X. Yang, *J. Electroanal. Chem.* **2013**, *688*, 93 – 97.
[19] R. S. Asher, *J. Inorg. Nucl. Chem.* **1959**, *10*, 238 – 249.
[20] P. Ge, M. Fouletier, *Solid State Ionics* **1988**, *28 – 30*, 1172 – 1175.
[21] M. Gu, A. Kushima, Y. Zhao, J. G. Zhang, J. Liu, N. D. Browning, J. Li, C. Wang, *Nano Lett.* **2013**, *13*, 5203 – 5211.
[22] L. L. Zhang, X. Zhao, M. D. Stoller, Y. Zhu, H. Ji, S. Murali, Y. Wu, S. Perales, B. Clevenger, R. S. Ruoff, *Nano Lett.* **2012**, *12*, 1806 – 1812.
[23] Y. Li, M. A. Trujillo, E. Fu, B. Patterson, L. Fei, Y. Xu, S. Deng, S. Smirnov, H. Luo, *J. Mater. Chem. A* **2013**, *1*, 12123 – 12127.
[24] J. C. Perez-Flores, A. Kuhn, F. García-Alvarado, *J. Power Sources* **2008**, *182*, 35 – 369.
[25] J. Shen, Y. Hu, M. Shi, X. Lu, C. Qin, C. Li, M. Ye, *Chem. Mater.* **2009**, *21*, 3514.
[26] H. Jung, C. M. Park, H. J. Sohn, *Electrochim. Acta* **2011**, *56*, 2135 – 2139.
[27] C. N. R. Rao, K. Biswas, K. S. Subramnayam, A. Govindaraj, *J. Mater. Chem.* **2009**, *19*, 2457.
[28] I. K. Moon, J. Lee, R. S. Ruoff, H. Lee, *Nat. Commun.* **2010**, *1*, 73.
[29] Q. Li, F. Zheng, Y. Huang, X. Zhang, Q. Wu, D. Fu, J. Zhang, J. Yin, H. Wang, *J. Mater. Chem. A* **2015**, *3*, 2025 – 2035.
[30] C. Gómez-Navarro, R. T. Weitz, A. M. Bittner, M. Scolari, A. Mews, M. Burghard, K. Kern, *Nano Lett.* **2007**, *7*, 3499 – 3503.
[31] M. A. Pimenta, G. Dresselhaus, M. S. Dresselhaus, L. G. Cancado, A. Jorio, R. Saito, *Phys. Chem. Chem. Phys.* **2007**, *9*, 1276.
[32] E. Strauss, G. Ardel, V. Livshits, L. Burstein, D. Golodnitsky, E. Peled, *J. Power Sources* **2000**, *88*, 206 – 218.
[33] Y. P. Wu, S. B. Fang, Y. Y. Jiang, *J. Power Sources* **1998**, *75*, 201.
[34] L. W. Ji, X. W. Zhang, *Electrochem. Commun.* **2009**, *11*, 1146 – 1149.
[35] I. A. Courtney, A. W. Wilson, J. R. Dahn, Abstract#66, 190th Meeting of the Electrochemical Society, San-Antonio, Texas, **1996**.
[36] C. M. Ban, Z. C. Wu, D. T. Gillaspie, L. Chen, Y. F. Yan, J. L. Blackburn, A. C. Dillon, *Adv. Mater.* **2010**, *22*, E145 – 149.
[37] G. M. Zhou, D. W. Wang, F. Li, L. L. Zhang, N. Li, Z. S. Wu, L. Wen, G. Q. Lu, H. M. Cheng, *Chem. Mater.* **2010**, *22*, 5306 – 5313.
[38] J. Z. Wang, C. Zhong, D. Wexler, N. H. Idlris, Z. X. Wang, L. Q. Chen, H. K. Liu, *Chem. Eur. J.* **2011**, *17*, 661 – 667.
[39] Y. Su, S. Li, D. Wu, F. Zhang, H. Liang, P. Gao, C. Cheng, X. Feng, *ACS Nano* **2012**, *6*, 8349 – 8356.
[40] X. Cheng, R. Li, Y. Sun, X. Q. Chen, D. Li, Y. Li, *Phys. Rev. B* **2014**, *89*, 245201 – 245205.
[41] L. Yue, H. Zhong, L. Zhang, *Electrochim. Acta* **2012**, *76*, 326 – 332.
[42] A. Yu, H. W. Park, A. Davies, D. C. Higgins, Z. Chen, X. Xiao, *J. Phys. Chem. Lett.* **2011**, *2*, 1855 – 1860.
[43] K. Yang, Z. Deng, J. Suo, *J. Power Sources* **2012**, *201*, 274 – 279.
[44] M. Shi, Z. Chen, J. Sun, *Cem. Concr. Res.* **1999**, *29*, 1111 – 1115.
[45] J. Zhu, T. K. Sharma, Z. Zeng, X. Zhang, M. Srinivasan, S. Mhaisalkar, H. Zhang, H. H. Hug, Q. Yan, *J. Phys. Chem. C* **2011**, *115*, 8400 – 8406.
[46] W. S. Hummers, R. E. Offeman, *J. Am. Chem. Soc.* **1958**, *80*, 1339 – 1339.
[47] X. Zhu, Y. Zhu, S. Murali, M. D. Stoller, R. S. Rouff, *ACS Nano* **2011**, *5*, 3333 – 3338.

Received: November 13, 2014
Revised: February 17, 2015